

SPECTROSCOPIC STUDIES OF Ho^{3+} -DOPED SrF_2 CRYSTAL OR GREEN AND RED LASER APPLICATIONS

Ravinder Kumar and David Joseph*

UDC 535.34;535.372

Spectroscopic studies of Ho^{3+} -doped SrF_2 crystals were performed regarding applications in solid-state lasers. The crystal structure of the $\text{Ho}:\text{SrF}_2$ crystal was investigated using single-crystal X-ray diffraction. SrF_2 exists as a cubic structure with an $Fm\bar{3}m$ space group. A Raman shift of 288 cm^{-1} was observed for the $\text{Ho}:\text{SrF}_2$ single crystal. SrF_2 hosts with low-frequency vibrational modes are suitable for reducing nonradiative emissions while maximizing radiative emissions. The absorption spectrum was recorded in the visible region from 400 to 800 nm, yielding absorption lines at 416, 450, 468, 473, 484, 536, 638, and 643 nm. The fluorescence spectrum recorded at an excitation wavelength of 450 nm shows two emission bands at 546 and 656 nm, which correspond to green and red emission, respectively. The intensity parameters Ω_λ ($\lambda = 2, 4$, and 6) were estimated using the Judd–Ofelt theory. For $\text{Ho}:\text{SrF}_2$ single crystal, the calculated Ω_λ are $\Omega_2 = 0.14 \times 10^{-20} \text{ cm}^2$, $\Omega_4 = 3.14 \times 10^{-20} \text{ cm}^2$, and $\Omega_6 = 3.74 \times 10^{-20} \text{ cm}^2$. The radiative transition probabilities, radiative lifetimes, and branching ratios β_R for $\text{Ho}:\text{SrF}_2$ were determined using the Judd–Ofelt parameters. The $^5S_2 + ^5F_4 \rightarrow ^5I_8$ transition is more effective for population-building processes because of its lifetime (0.26 ms) and higher branching ratios (~82.86%). $\text{Ho}:\text{SrF}_2$ is, therefore, a promising solid-state laser crystal for green and red spectral regions.

Keywords: single crystal, phonon, absorption, emission, fluorescence, solid-state laser, oscillator strength, Judd–Ofelt theory, transition probabilities, radiative lifetime, branching ratios.

Introduction. Lasers operating in the visible spectrum region are extensively used in laser spectroscopy, nonlinear optics, and coherent control equipment. It has been observed experimentally that rare-earth (RE) group elements provide an efficient gain medium for solid-state lasers in the visible range. RE ions are transparent when doped into crystals, glasses, and fibers, with sharp optical transitions. However, the crystal environment produces a broadening of the emission lines. In previous studies, Er^{3+} [1, 2], Tm^{3+} [3], Dy^{3+} [4, 5], Sm^{3+} [6], Tb^{3+} [7], and Ho^{3+} [8] have shown laser operation in the visible region. Compared to all RE ions, the holmium ion (Ho^{3+}) is well recognized because of its multiple metastable levels. They can exhibit laser emission from the visible to infrared spectral regions [8, 9]. Large population inversion can be achieved at relatively long-lived 5I_7 levels of Ho^{3+} ions [10] and has shown an emission of approximately $2 \mu\text{m}$ from the 5I_7 to 5I_8 transition. Therefore, this laser wavelength is safe for the eyes and is used in the medical treatment of the eyes. During the transition from $^5F_4, ^5S_2$ to 5I_8 , a green-wavelength emission at 545 nm has been observed [11]. A red-wavelength emission at 663 nm is recorded for the transition from 5F_5 to 5I_8 [12, 13]. The host material, SrF_2 , affects the spectroscopic transitions of Ho^{3+} because of the phonon modes of the host. In rare-earth-doped materials, the emission quantum efficiency is dependent on the phonon energy of the host matrix; hence, the selection of the host material is crucial for the exploration of luminescence features. The SrF_2 crystal has a prominent vibrational mode at 282 cm^{-1} [14]; furthermore, the low-phonon energy host is favorable for Ho^{3+} ions since a few of the energy levels in Ho^{3+} have an energy gap of approximately 1000 cm^{-1} . Nonradiative emissions can be reduced and radiative emissions can be increased in a host material with low phonon energy [15]; thus, it is crucial to select a host material with low lattice vibrational modes. However, crystal field splitting due to the host atoms may be observed. In the present work, a SrF_2 single crystal is selected as the host material for Ho^{3+} ions. The crystal structure of $\text{Ho}:\text{SrF}_2$ is confirmed using single-crystal X-ray diffraction (XRD). SrF_2 is a member of the fluoride MF_2 family ($M = \text{Ca}, \text{Sr}$, and Ba). The structures of these fluorides are fluorite-like, with symmetry O_h^5 and space group $Fm\bar{3}m$.

*To whom correspondence should be addressed.

Department of Physics, Guru Jambheshwar University of Science & Technology, Hisar, Haryana, India; email: davidjp707@gmail.com. Abstract of article is published in Zhurnal Prikladnoi Spektroskopii, Vol. 91, No. 4, p. 603, July–August, 2024.

Our crystal (SrF_2) has a cubic crystal structure with a lattice constant of 5.7928 Å. The absorption spectra were measured from 400 to 800 nm and absorption peaks were observed at 416, 450, 468, 473, 484, 536, 638, and 643 nm. The emission spectrum was recorded at an excitation wavelength of 450 nm. Two emission bands corresponding to the green and red wavelength regions were observed at 546 nm and 656 nm, respectively. Furthermore, we calculated the Judd–Ofelt (J–O) intensity parameters Ω_2 , Ω_4 , and Ω_6 from the room temperature absorption spectra using the J–O theory. The radiative transition probabilities (A_R), branching ratios (β_R), and radiative lifetimes (τ_R) of various excited states of the Ho^{3+} ion in the SrF_2 single crystal were calculated based on the obtained J–O intensity parameters.

Experimental. The X-ray diffraction (XRD) pattern was recorded using a Supernova, a single source, at an offset Hypix 3000 diffractometer. Monochromatic MoK_α was used as an X-ray source with $\lambda = 0.71073$ Å. Raman spectroscopy is used to study the vibrational modes of the SrF_2 host lattice, which has a cubic lattice. Raman spectra were recorded using a Raman spectrophotometer (WITEC alpha 300 Ri). A diode laser with a wavelength of 785 nm was used as an excitation source. LAMBDA 750 UV-Vis NIR Spectrophotometer (Perkin Elmer) was used to record the UV-visible spectrum in the visible spectral wavelength range of 400 to 800 nm. LS 55 (Perkin Elmer) fluorescence spectrometer was used to record the emission spectrum at an excitation wavelength of 450 nm.

Results and Discussion. The structure of the $\text{Ho}:\text{SrF}_2$ crystal is determined by single crystal XRD using monochromatic MoK_α , having $\lambda = 0.71073$ Å. During the data collection, the crystals were maintained at 293 K. The data collection spans a 2θ range from 12.20 to 52.52°. The structure was solved using intrinsic phasing in the ShelXT structural solving program [16]. The olex2.refine refinement program was used to refine the XRD data [17]. In olex2.refine, refinement was performed using Gauss–Newton minimization [18]. The $\text{Ho}:\text{SrF}_2$ crystal was confirmed as having cubic symmetry, and the unit cell parameters obtained are $a = 5.7928(3)$ Å, $b = 5.7928(3)$ Å, and $c = 5.7928(3)$ Å. It has a space group of $Fm\bar{3}m$ and a volume of 194.386 Å³. The VESTA program was used to model the SrF_2 unit cell. The lattice parameters and atomic position coordinates were found by refining the XRD data, which can be seen in Fig. 1. The coordination number of the Sr ions obtained is 8 and that of the fluorine ion is 4. Sr^{2+} is connected to eight equivalent F^{1-} atoms in a body-centered cubic shape. The length of all Sr–F bonds is 2.5084 Å. The bonding of F^{1-} to four equivalent Sr^{2+} atoms creates an FSr_4 tetrahedron. The fractional atomic coordinates, equivalent isotropic displacement parameters, and atomic occupancies are listed in Table 1. Table 2 lists the unit cell dimensions, additive crystallographic data, and refinement results. The XRD results for the single crystals agree well with the reported values and thus confirm the structure of the $\text{Ho}:\text{SrF}_2$ crystal [14].

Analysis of the Raman spectrum determines the lattice vibrational mode of the SrF_2 host matrix. A diode laser source with 785 nm excitation was used to record Raman spectra. Three atoms in the primitive cubic cell of SrF_2 generate nine fundamental vibrational modes. These modes are defined as $\Gamma_9 = 2F_{1u} + F_{2g}$, which is the irreducible representation (at $k = 0$) of the symmetry group O_h^5 [19]. F_{2g} is a triply degenerate optical mode. There are two types of F_{1u} representations: triply degenerate and zero-acoustical mode [20]. The other is doubly degenerate and represents the transverse optical mode and the nondegenerate longitudinal optical mode. All F_{1u} representations are IR-active and Raman-inactive, in contrast to the F_{2g} representation, which is Raman-active and IR-inactive [14]. This vibrational mode (F_{2g}) of undoped SrF_2 is Raman-active, with ω at 282 cm⁻¹ [14]. In this mode, the F^{1-} anions moved closer to each other along the crystallographic axes, a phenomenon related to the excited fluorine sublattice of SrF_2 . The Raman spectra of the Ho^{3+} -doped SrF_2 are shown in Fig. 2. A Raman shift with a phonon frequency of 288 cm⁻¹ is observed for Ho-doped SrF_2 . The Raman shift towards a higher wavenumber in $\text{Ho}:\text{SrF}_2$ may be due to the change in the chemical environment around the F^{1-} ion when Ho is doped in the SrF_2 host matrix. Thus, the low-energy vibrational mode of SrF_2 makes it suitable for Ho-doped lasers. It is well understood that a system with relatively low phonon energies can boost radiative emissions while reducing nonradiative emissions [15]. This is because lower phonon energy reduces nonradiative transitions, which increases the fluorescence intensity.

Absorption spectra were obtained in the 400–800 nm wavelength range, as shown in Fig. 3. The 4f–4f transition of Ho^{3+} accounted for the observed absorption lines in the visible region. The absorption lines were observed at 416, 450, 468, 473, 484, 536, 638, and 643 nm. Table 3 compares the observed absorption wavelengths with previously published absorption spectra [8, 21]. Among all the observed peaks, the absorption transition from 5I_8 to 5G_6 is very sensitive to the surrounding environment of the Ho^{3+} ions. Transitions 5I_8 to 5G_6 follow the selection rules $\Delta J \leq 2$, $\Delta L \leq 2$, and $\Delta S = 0$ [22]. The transition from 5I_8 to 5G_5 corresponds to violet light absorption, and 5I_8 to 5F_1 , 5G_6 , 3K_8 , 5F_2 , and 5F_3 corresponds to blue light absorption peaks. The transitions from 5I_8 to 5S_2 , 5F_4 , and 5I_8 to 5F_5 show green and red lights, respectively. The intensity of the absorption line is calculated as a function of oscillator strength f_{exp} using the expression [23, 24]:

$$f_{\text{exp}} = 4.32 \times 10^{-9} \int \epsilon(v) d(v), \quad (1)$$

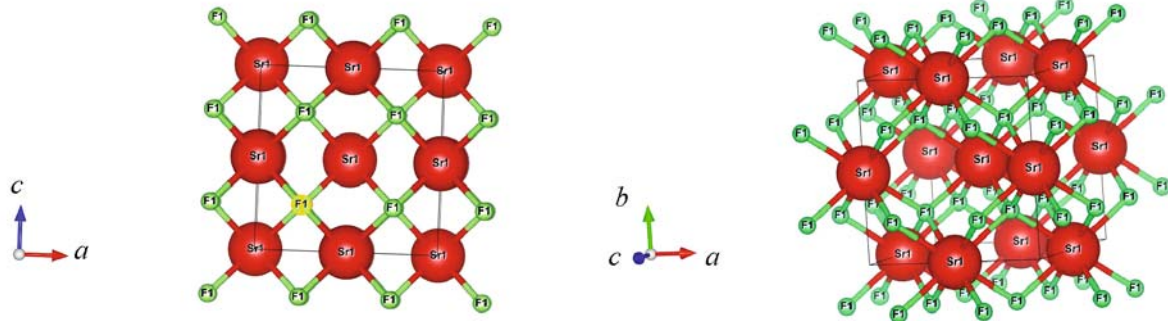


Fig. 1. Unit cell of sample SrF_2 as modeled by VESTA.

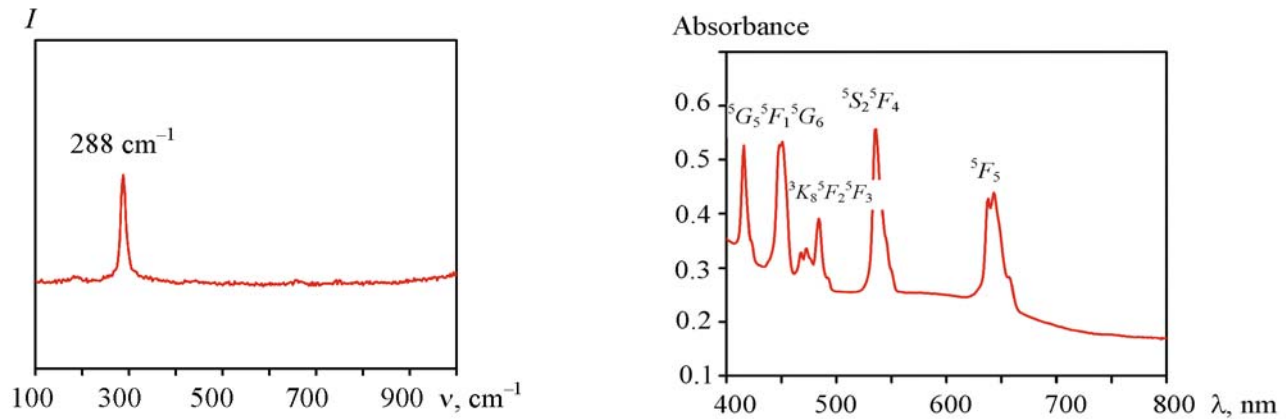


Fig. 2. Raman spectrum of Ho:SrF_2 .

Fig. 3. Absorption spectrum of Ho:SrF_2 showing absorption transitions of Ho^{3+} ion.

TABLE 1. Fractional Atomic Coordinates ($\times 10^{-4}$) Equivalent Isotropic Displacement Parameters ($\text{\AA}^2 \times 10^3$) and Atomic Occupancy for Ho-SrF_2 . U(eq) Is Defined as 1/3 of the Trace of the Orthogonalised UIJ Tensor

Atom	<i>x</i>	<i>y</i>	<i>z</i>	U(eq)	Occupancy
Sr1	5000	5000	5000	10.9(7)	0.999840
F1	2500	2500	2500	14.1(18)	1.000080

where $\epsilon(v)$ is the molar extinction coefficient at wavenumber (v , cm^{-1}). As can be observed from Table 4, the transitions ${}^5I_8 \rightarrow {}^5S_2$, and 5F_4 have the highest oscillator strengths (5.50×10^{-6}), whereas the transitions ${}^5I_8 \rightarrow {}^3K_8$ have the lowest oscillator strengths (1.23×10^{-6}). Oscillator strength (f_{cal}) can also be determined for an induced electric-dipole transition from the ground state ΨJ to an excited state $\Psi J'$ using the J–O theory. The electric dipole transition between $4f^n$ states of rare earth ions has an oscillator strength per the J–O theory and is calculated using the following formula [25]:

$$f_{\text{cal}} = v/(2J + 1) \left[\left(8\pi^2 mc (n^2 + 2)^2 \right) / 27nh \right] \sum_{\lambda=2,4,6} \Omega_\lambda \langle |\Psi J | U^\lambda | \Psi J' \rangle^2, \quad (2)$$

where v is the wavenumber of the transition, n is the refractive index of the material, J is the total angular momentum of the ground state, and J' is the total angular momentum of the excited state, Ω_λ ($\lambda = 2, 4$, and 6) are the J–O intensity

TABLE 2. Crystal Data and Structure Refinement for Ho:SrF₂

Identification code	Ho-SrF ₂
Empirical formula	F _{2.67} Sr _{1.33}
Formula weight	167.47
Temperature, K	293
Crystal system	cubic
Space group	<i>Fm</i> 3 <i>m</i>
<i>a</i> , Å	5.7928(3)
<i>b</i> , Å	5.7928(3)
<i>c</i> , Å	5.7928(3)
α, °	90
β, °	90
γ, °	90
Volume, Å ³	194.386(17)
<i>Z</i>	3
ρ _{calc} , g/cm ³	4.2916
μ, mm ⁻¹	27.368
<i>F</i> (000)	218.1
Radiation	Mo <i>K</i> _α (λ = 0.71073)
2θ range for data collection, °	12.2 to 52.52
Index ranges	-7 ≤ <i>h</i> ≤ 7, -7 ≤ <i>k</i> ≤ 5, -7 ≤ <i>l</i> ≤ 6
Reflections collected	445
Independent reflections	22 [Rint = 0.1070, Rsigma = 0.0261]
Data/restraints/parameters	22/0/2
Goodness-of-fit on F ²	1.023
Final <i>R</i> indices [<i>I</i> ≥ 2σ(<i>I</i>)]	R1 = 0.0226, wR2 = 0.0510
Final <i>R</i> indices [all data]	R1=0.0226, wR2=0.0510
Largest diff. peak/hole/e, Å ⁻³	0.43/-0.65

parameters, and $U^\lambda = |\langle \Psi J | U^\lambda | \Psi J' \rangle|^2$ are the doubly reduced matrix elements of the unit tensor operator. The f_{exp} and f_{cal} values were matched well for each transition, as shown in Table 4. In a previous study, Carnal et al. provided host-independent doubly reduced matrix elements for Ho³⁺ ions [26]. For each spectral transition, one can compare Eqs. (1) and (2) and then use the least-squares fitting method to obtain the Ω_λ values. These three intensity characteristics are the causes of the range of transition intensities. The calculated values for the J-O intensity parameters are $\Omega_2 = 0.14 \times 10^{-20}$ cm², $\Omega_4 = 3.14 \times 10^{-20}$ cm², and $\Omega_6 = 3.74 \times 10^{-20}$ cm². It is important to note that the Ω_2 value for the crystal is low and follows the order $\Omega_2 < \Omega_4 < \Omega_6$. Ω_2 is affected by ligand field covalence, structural change, and asymmetry around the RE³⁺ site, whereas Ω_4 and Ω_6 measure the rigidity of the host medium [27–29]. The low value of Ω_2 and the trend of $\Omega_2 < \Omega_4 < \Omega_6$ for Ho³⁺ ions in SrF₂ suggest that the surrounding Ho³⁺ site is comparatively highly symmetric, whereas the Ho-F bond is less covalent.

The observed ground-state absorption spectrum was utilized to estimate the excitation wavelength for the emission spectrum using the reciprocity approach [23, 24]. The emission spectra of Ho:SrF₂ were recorded at an excitation wavelength

TABLE 3. Comparison of Absorption Spectrum (λ , nm) of Ho-doped SrF₂ with [8] and [21]

Transition from 5I_8 to	Observed absorption wavelength, nm	Absorption wavelength [8], nm	Absorption wavelength [21], nm
5G_5	416	418	—
$^5F_1, ^5G_6$	450	448	449.9, 452.9
3K_8	468	—	468
5F_2	473	—	473
5F_3	484	485	484.5, 486
$^5S_2, ^5F_4$	536	537	537.3, 535.2
5F_5	638, 643	642	—

 TABLE 4. Reduced Matrix Elements, f_{exp} and f_{cal} of Ho:SrF₂ Crystal

Transition from 5I_8 to	Wavenumber, cm ⁻¹	U^2	U^4	U^6	$f_{\text{exp}}, 10^{-6}$	$f_{\text{cal}}, 10^{-6}$
5G_5	24,038	0	0.5338	0.0002	3.80	3.30
$^5F_1, ^5G_6$	22,223	1.5201	0.841	0.1411	5.36	5.36
3K_8	22,295	0.0208	0.0334	0.1578	1.23	1.26
5F_2	21,141	0	0	0.1921	1.25	1.24
5F_3	20,652	0	0	0.346	2.66	2.18
$^5S_2, ^5F_4$	18,613	0	0.2392	0.7071	5.50	5.16
5F_5	15,532	0	0.425	0.5687	3.81	4.38

of 450 nm, as shown in Fig. 4a. Green and red lights emissions occur with blue-light pumping. Ho³⁺ ions were initially stimulated from the ground state 5I_8 to the excited state 5G_6 , as depicted in Fig. 4b. Following this, because of the closely spaced higher energy levels, both radiative and nonradiative relaxations occurred. The excited electrons at the 5G_6 level populate the 5S_2 , 5F_4 , and 5F_5 levels via nonradiative relaxation. The emission spectrum exhibits two emission lines at 546 nm (green) and 656 nm (red). The emission line at 546 nm correlates with the transition from 5S_2 to 5F_4 to 5I_8 , whereas the emission line at 656 nm is related to the transition from 5F_5 to 5I_8 . The emission peaks of 5S_2 , 5F_4 , 5I_8 , 5I_8 , 5S_2 , and 5F_4 match each other, that is, their wavelengths lie between 525 and 553 nm. The 5F_5 to 5I_8 emission band matches the absorption band 5I_8 to 5F_5 , that is, their wavelengths lie between 624 and 664 nm, which is an evidence of the resonance energy-transfer mechanism [8]. According to the emission spectra, the intensities of the 5S_2 , 5F_4 , and 5I_8 transitions are greater than those of the 5F_5 and 5I_8 transitions. This variation in intensity can be attributed to different multiphonon relaxation modes. The rate of multiphonon relaxation increases as the energy difference between the excited state and the lower-lying state narrows [25]. The excited states 5S_2 and 5F_4 have an energy gap of approximately 2900 cm⁻¹ from their lower-lying energy levels [20], while the energy gap from the lower-lying level to the 5F_5 excited state is approximately 1704 cm⁻¹ [8]. As a result, compared with the 5F_5 to 5I_8 transition, the 5S_2 to 5F_4 to 5I_8 transition gains more populated excited states and less multiphonon relaxation; thus, green light emission is more intense than red light. The emission lines confirm that the Ho:SrF₂ crystal is a potent candidate as a laser medium in green and red light.

The spontaneous emission probability A_R ($A_{jj'}$), fluorescence branching ratio β_R , and radiative lifetime τ_R are calculated using the J-O intensity parameters using the following formulas [30]:

$$A_R = \frac{64\pi^4 v^3 e^2 n (n^2 + 2)^2}{27h(2J+1)} \sum_{\lambda=2,4,6} \Omega_\lambda \left| \langle \Psi J | U^\lambda | \Psi J' \rangle \right|^2, \quad (3)$$

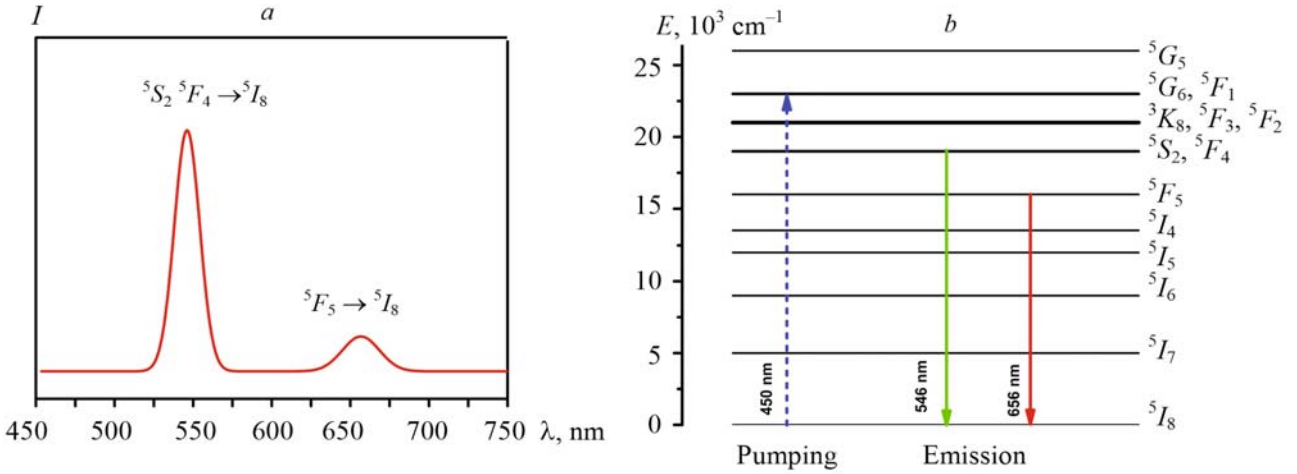


Fig. 4. (a) Fluorescence spectrum and (b) Schematic diagram of emission spectrum of Ho:SrF₂.

TABLE 5. The Predicted Radiative Transition Probability A_R , Total Radiative Transition Probability A_T , Calculated Branching Ratio β_R and Radiative Lifetime τ_R of the Energy Levels of Ho³⁺ Ion in Ho-doped SrF₂ Crystal [34]

Transition	v, cm ⁻¹	Matrix elements			A_R, s^{-1}	A_T, s^{-1}	$\beta_R, \%$	τ_R, ms
		U^2	U^4	U^6				
$^5S_2 + ^5F_4 \rightarrow ^5I_8$	18.315	0.0000	0.2421	0.7087	3135.89	3784.60	82.86	0.26
5I_7	13,499	0.0000	0.1960	0.0322	272.54		7.20	
5I_6	9919	0.0011	0.2576	0.1721	213.29		5.63	
5I_5	7493	0.0016	0.1327	0.4651	136.36		3.60	
5I_4	5429	0.0002	0.0237	0.2585	25.03		0.66	
5F_5	3066	0.2001	0.0919	0.0075	1.49		0.04	
$^5F_5 \rightarrow ^5I_8$	15.244	0.0000	0.4241	0.5698	1508.73	1978.24	76.27	0.50
5I_7	10.433	0.0190	0.3318	0.4346	373.07		18.86	
5I_6	6853	0.0112	0.1242	0.4960	88.92		4.49	
5I_5	4427	0.0068	0.0279	0.1637	7.47		0.38	
5I_4	2363	0.0001	0.0060	0.0040	0.05		0.25×10^{-2}	

$$\beta_R = \frac{A_{JJ'}}{\sum_J A_{JJ'}}, \quad (4)$$

$$\tau_R = \frac{1}{\sum_J A_{JJ'}}. \quad (5)$$

Using Eqs. (3)–(5), the calculated values of the emission transition parameters like emission probability A_R , fluorescence branching ratio β_R , and radiative lifetime τ_R are tabulated in Table 5. The transition probability is the highest for the $^5S_2 + ^5F_4 \rightarrow ^5I_8$ transition. The term "lifetime" refers to the period after which the population level has decreased to 36.8% of the initial population. The $^5S_2 + ^5F_4 \rightarrow ^5I_8$ transition is the most effective for lasing, owing to its lifetime of 0.26 ms. The computed branching ratios of 82.86% and 76.27% for the $^5S_2 + ^5F_4 \rightarrow ^5I_8$ and $^5F_5 \rightarrow ^5I_8$ transitions, respectively, are in good

agreement with [31–33]. Emission transitions with larger magnitudes of β_R are better suited for laser action, as β_R denotes a more effective transition for laser action. Consequently, a transition with a fluorescence branching ratio greater than 50% is appropriate for lasing [8]. Thus, green and red emissions can be obtained as laser transitions in Ho:SrF₂.

Conclusions. In the present work, the Ho-doped SrF₂ crystal was investigated as a gain medium for solid-state lasers in the visible spectral band. The crystal structure of the Ho:SrF₂ crystal was confirmed using single-crystal XRD. Olex2 software was used to solve the structure by utilizing intrinsic phasing with the ShelXT structure solution tool. The olex2 refine software was used to refine the XRD data using Gauss–Newton minimization. SrF₂ has a cubic structure with a lattice constant $a = 5.7928 \text{ \AA}$. A lattice vibrational mode of 288 cm⁻¹ is observed in the Ho:SrF₂ single crystal via Raman spectroscopy, which is a suitable environment for fluorescence intensity by limiting nonradiative transitions. The UV-visible absorption spectrum was recorded in the 400–800 nm region and different absorption lines were observed at wavelengths of 416, 450, 468, 473, 484, 536, 638, and 643 nm. The emission spectrum was studied using fluorescence spectroscopy at an excitation wavelength of 450 nm. Two emission bands were observed: one at 546 nm corresponds to the green-light region, and the second at 656 nm corresponds to the red-light region. The intensity parameters $\Omega_\lambda (\lambda = 2, 4, 6)$ were estimated using Judd–Ofelt's theory. The low Ω_2 value in the Ho:SrF₂ single crystal suggests low covalence of Ho³⁺–F⁻ bonds and high ligand field symmetry around Ho³⁺ ion sites. The radiative properties of various excited levels were predicted using the measured Judd–Ofelt's intensity values. The $^5S_2 + ^5F_4 \rightarrow ^5I_8$ transition has a shorter lifespan (0.26 ms) and a higher branching ratio (82.86%), making it more suitable for lasing. Thus, Ho:SrF₂ can be a promising crystal as a laser in the green and red spectral regions.

Acknowledgments. The authors acknowledge Dr. Subhash Chandra Sahoo, Department of Chemistry, Punjab University Chandigarh, for recording single crystal XRD measurements and the Material Research Center, Malaviya National Institute of Technology (MNIT), Jaipur, for measurements of photoluminescence and the UV-visible spectrum.

REFERENCES

1. T. Danger, J. Koetke, R. Brede, E. Heumann, G. Huber, and B. H. T. Chai, *Appl. Phys.*, **76**, 1413–1422 (1994).
2. F. Moglia, S. Müller, T. Calmano, and G. Huber, *5th EPS-QEOD Europhoton Conf. 2012*, Stockholm, Sweden, **25** (2012).
3. B. P. Scott, F. Zhao, R. S. F. Chang, and N. Djeu, *Opt. Lett.*, **18**, 113–115 (1993).
4. S. R. Bowman, S. O'Connor, and N. J. Condon, *Opt. Express*, **20**, 12906–12911 (2012).
5. P. W. Metz, F. Moglia, F. Reichert, S. Müller, D.-T. Marzahl, N.-O. Hansen, C. Kränel, and G. Huber, *Conf. on Lasers and Electro-Optics (CLEO/Europe — EQEC) 2013*, Munich, Germany, paper: CA-2.5 (2013).
6. B. N. Kazakov, M. S. Orlov, M. V. Petrov, A. L. Stolov, and A. M. Tkachuk, *Opt. Spectrosc.*, **47**, 676 (1979).
7. H. Jensen, D. Castleberry, D. Gabbe, and A. Linz, *IEEE J. Quantum Electron.*, **9**, 665 (1973).
8. P. Rekha Rani, M. Venkateswarlu, Sk. Mahamuda, K. Swapna, Nisha Deopa, and A. S. Rao, *J. Alloys Compd.*, **787**, 503–518 (2019).
9. Wenqian Cao, Feifei Huang, Tao Wang, Renguang Ye, Ruoshan Lei, Ying Tian, Junjie Zhang, and Shining Xu, *Opt. Mater.*, **75**, 695–698 (2018).
10. M. Kochanowicz, J. Zmojda, P. Miluski, A. Baranowski, M. Leich, A. Schwuchow, M. Jeager, M. Kuwik, J. Pisarska, W. A. Pisarski, and D. Dorosz, *Opt. Mater. Express*, **9**, 1450–1458 (2019).
11. E. Chicklis, C. Naiman, L. Esterowitz, and R. Allen, *IEEE J. Quantum Electron.*, **13**, 893–895 (1977).
12. J. Y. Allain, M. Monerie, and H. Poignant, *Electron. Lett.*, **26**, 261–263 (1990).
13. David S. Funk and J. G. Eden, *IEEE J. Quantum Electron.*, **37**, 980–992 (2001).
14. A. A. Kaminski, L. Bahaty, P. Becker, H. J. Eichler, and H. Rhee, *Laser Phys. Lett.*, **4**, 668–673 (2007).
15. Bingrui Li, Xin Zhao, Edwin Yue Bun Pun, and Hai Lin, *Opt. Laser Technol.*, **107**, 8–14 (2018).
16. G. M. Sheldrick, *Acta Cryst. A*, **71**, 3–8 (2015).
17. L. J. Bourhis, O. V. Dolomanov, R. J. Gildea, J. A. K. Howard, and H. Puschmann, *Acta Cryst. A*, **71**, 59–75 (2015).
18. O. V. Dolomanov, L. J. Bourhis, R. J. Gildea, J. A. K. Howard, and H. Puschmann, *J. Appl. Cryst.*, **42**, No. 2, 339–341 (2009).
19. R. L. Rousseau, R. P. Baumann, and S. P. S. Porto, *J. Raman Spectrosc.*, **10**, No. 1, 253 (1981).
20. G. A. Kourouklis, E. Anastassakis, *Phys. Rev. B*, **34**, 1233 (1986).
21. F. Reichert, F. Moglia, P. W. Metz, A. Arcangeli, D.-T. Marzahl, S. Veronesi, D. Parisi, M. Fechner, M. Tonelli, and G. Huber, *Opt. Mater. Express*, **5**, 88–101 (2014).

22. D. Rajesh, M. Dhamodhara Naidu, Y. C. Ratnakaram, and A. Balakrishna, *J. Lumin.*, **29**, No. 7, 854–860 (2014).
23. B. R. Judd, *Phys. Rev.*, **127**, 750 (1962).
24. G. S. Ofelt, *J. Chem. Phys.*, **37**, 511–520 (1962).
25. R. D. Peacock, *Structure & Bonding*, **22**, 83 (1975).
26. W. T. Carnall, P. R. Fields, and K. Rajnak, *J. Chem. Phys.*, **49**, 4412 (1968).
27. S. Tanabe, T. Ohayagi, N. Soga, and T. Hanada, *Phys. Rev. B*, **46**, 3305 (1992).
28. H. Ebendorff-Heidepriem, D. Ehrt, M. Bettinelli, and A. Speghini, *J. Non-Cryst. Solids*, **240**, 66 (1998).
29. H. Takebe, Y. Nagano, and K. Morinaga, *J. Am. Ceram. Soc.*, **78**, 61 (1995).
30. B. M. Walsh, P. B. Norman, and D. B. Baldassare, *J. Appl. Phys.*, **83**, 2772 (1998)
31. V. D. Rodríguez, J. Del Castillo, A. C. Yanes, J. Méndez-Ramos, M. Torres, and J. Peraza, *Opt. Mater.*, **29**, 1159 (2007).
32. J. Peng, H. Xia, P. Wang, H. Hu, L. Tang, Y. Zhang, H. Wang, and B. Zhang, *J. Mater. Sci. Technol.*, **30**, 910 (2014).
33. R. S. Quimby, N. J. Condon, S. P. O'Connor, and S. R. Bowman, *Opt. Mater.*, **34**, 1603 (2012).
34. H. M. Ha, T. T. Q. Hoa, L. V. Vu, and N. N. Long, *J. Mater Sci.: Mater. Electron.*, **29**, 1607–1613 (2018).